



Cite this: DOI: 10.1039/c6ta09645j

# Direct deposition of MoSe<sub>2</sub> nanocrystals onto conducting substrates: towards ultra-efficient electrocatalysts for hydrogen evolution†

Dijo Damien,<sup>a</sup> Athira Anil,<sup>a</sup> Dipanwita Chatterjee<sup>b</sup> and M. M. Shaijumon \*<sup>a</sup>

There is an urgent need to develop efficient and cost-effective catalysts for the hydrogen evolution reaction (HER) in order to realize a hydrogen economy with clean and renewable energy. Nanostructures of layered transition metal dichalcogenides show promising electrocatalytic activity towards the hydrogen evolution reaction, however, the majority of the exposed surfaces (basal planes) are inactive, and engineering their catalytically active edge sites still remains a challenge. Here we show that monodisperse single/few-layered MoSe<sub>2</sub> nanocrystals can be directly deposited onto any conducting substrate, through electrochemical exfoliation of bulk MoSe<sub>2</sub>, which exhibit remarkable electrocatalytic activity for the HER with ultra-high efficiency showing a very low on-set potential (70.9 mV vs. the RHE) and Tafel slope (31.8 mV dec<sup>-1</sup>). The exceptional electrocatalytic activity of the MoSe<sub>2</sub> nanocrystals results from the synergistic advantages emerging from improved edge sites, enhanced electronic conductivity and the presence of new and active sites arising upon *in situ* lithiation, all in one step, which is facile, economic and environmentally benign.

Received 8th November 2016  
Accepted 31st March 2017

DOI: 10.1039/c6ta09645j

rsc.li/materials-a

## Introduction

Hydrogen is a clean energy carrier and exhibits the highest specific energy among all fuels and hence is regarded as an ideal candidate for meeting future fuel needs.<sup>1</sup> Among several techniques available for hydrogen production, electrolytic/photolytic water splitting is being regarded as the most economical and environmentally benign process.<sup>2</sup> Electrocatalysts minimize the energy requirement for water splitting by driving the reaction through an energetically favorable kinetic pathway. Pt and other noble metals are the best electrocatalysts for the hydrogen evolution reaction (HER).<sup>3</sup> Recently, there are a few reports on non-noble metal based electrocatalysts, such as CoP nanocrystals,<sup>4</sup> CoPS,<sup>5,6</sup> Cu–Ti bimetallic systems,<sup>7</sup> Ni–Mo alloys<sup>8</sup> and 2D-FePS<sub>3</sub><sup>9</sup> possessing comparable catalytic activities to that of Pt; however, many of them are not stable under acidic conditions. The search for earth abundant alternatives to Pt-based catalysts sheds light on dichalcogenides of molybdenum and tungsten through a biomimetic approach along computational predictions,<sup>10</sup> and has received great attention in recent times.

Irrespective of the choice of chalcogenide (S<sup>2-</sup>/Se<sup>2-</sup>), all the dichalcogenides of Mo and W have an electrochemically inert basal plane (0001) because of high  $\Delta G_{\text{H}} \sim 2$  eV. Initial research on TMD-based electrocatalysts was focused on addressing basal plane activity and conductivity issues.<sup>11</sup> Vertically aligned growth,<sup>12–14</sup> morphology engineering,<sup>15,16</sup> and defect-rich/amorphous nanostructures<sup>17–20</sup> were proposed to enhance the edge to basal plane ratio. Modifying TMD nanostructures *via* chemical doping,<sup>21–23</sup> making core–shell nanostructures,<sup>24–26</sup> preparation of composites with graphene,<sup>27–29</sup> *etc.* were the strategies developed for enhancing the conductivity. These methods certainly improved their catalytic efficiency towards the HER; however, they are found to be inadequate to replace Pt. Very recently, Brinker and co-workers reported that this enhancement in catalytic efficiency stems from the incomplete phase transformation and the presence of catalytically active basal planes of a distorted phase named as 1T', where  $\Delta G_{\text{H}}$  for the basal plane is found to be significantly reduced to 0.18 eV from  $\sim 2$  eV.<sup>30</sup> Cummins *et al.* recently reported that Li-treated core–shell MoO<sub>x</sub>/MoS<sub>2</sub> nanowires outperform 1T-MoS<sub>2</sub> sheets by virtue of an increased concentration of defect sites, instead of the crystal phase transformation.<sup>25</sup> All these efforts were focused on MoS<sub>2</sub>. However, the criterion of thermoneutrality makes MoSe<sub>2</sub> and WS<sub>2</sub> the most eligible electrocatalysts among TMDs, as both their metal and chalcogenide edges are catalytically active compared to MoS<sub>2</sub> and WSe<sub>2</sub>.<sup>31,32</sup> Apart from the thermoneutral chemistry, MoSe<sub>2</sub> has another advantage in terms of its band structure compared to its disulphide analogue. Thermodynamically stable bulk MoSe<sub>2</sub> has a band

<sup>a</sup>Indian Institute of Science Education and Research Thiruvananthapuram, Thiruvananthapuram, Kerala, 695016, India. E-mail: shaiju@iisertvm.ac.in

<sup>b</sup>Materials Research Center, Indian Institute of Science, Bangalore, Karnataka, 560012, India

† Electronic supplementary information (ESI) available: Microscopic and spectroscopic characterization, EDX, electron diffraction data, *etc.* See DOI: 10.1039/c6ta09645j

gap of 1.05 eV, with better electronic conductivity and its conduction band minimum is placed much lower than that of 2H-MoS<sub>2</sub>, which is well above the water reduction potential.<sup>33</sup> However, the catalytic activity of MoSe<sub>2</sub> is also limited to the edge plane, similar to MoS<sub>2</sub>.<sup>13</sup>

Here we report, for the first time, a facile approach for direct deposition of monodisperse single/few-layered MoSe<sub>2</sub> nanocrystals onto conducting substrates, through electrochemical exfoliation of bulk MoSe<sub>2</sub>. With the synergistic advantages arising from improved edge sites, enhanced electronic conductivity and the presence of lithiated molybdenum selenide nanocrystals, the material exhibits exceptional electrocatalytic activity towards the HER with ultra-high efficiency. Considering the fact that the electrode fabrication technique is critical for the catalytic performance, we compare the electrocatalytic activity of MoSe<sub>2</sub> nanocrystals fabricated by dropcasting, self-assembly (SA) and electrophoretic deposition (ED) onto a gold electrode.

## Experimental

### Synthesis of MoSe<sub>2</sub> nanocrystals

MoSe<sub>2</sub> nanocrystals were synthesized through an electrochemical route by slightly modifying our earlier protocol.<sup>34,35</sup> MoSe<sub>2</sub> flakes (Alfa Aesar) and lithium bis(trifluoromethane)sulfonimide (LiTFSI) salt (Sigma-Aldrich) were used as received. In a typical synthesis, 500 mg of MoSe<sub>2</sub> powder was pelletized by applying a pressure of 5 tons per cm<sup>2</sup>. This pellet of diameter 10 mm was employed as an anode and conducting substrates of choice *viz.* gold, fluorine doped tin oxide (FTO) coated glass, *etc.* of dimension 2 × 10 mm were used as cathodes for the electrochemical exfoliation. The electrodes were placed in an electrochemical cell 1 cm apart, in 0.1 wt% aq. LiTFSI electrolyte. The photograph of the experimental setup used is shown in Fig. S1.† A constant DC potential of 5 V is applied across the electrodes at room temperature. The electrolyte containing exfoliated MoSe<sub>2</sub> nanocrystals was collected after 24 h and centrifuged using Vivaspin 2 centrifugal concentrators (Sigma-Aldrich) at 6000 rpm for 1 h to remove any traces of bulk MoSe<sub>2</sub>. The total solid content of the exfoliation mixture was found to be 1.82 mg mL<sup>-1</sup> before centrifugation which was reduced to 1.60 mg mL<sup>-1</sup> after centrifugation. The cathode electrophoretically coated with MoSe<sub>2</sub> nanocrystals was washed with ethanol followed by with DI water and dried in a vacuum desiccator for 48 h.

### Materials characterization

The exfoliated MoSe<sub>2</sub> nanocrystals and coated substrates were characterized using various microscopic and spectroscopic tools, including a high resolution transmission electron microscope (HR-TEM), an atomic force microscope (AFM), an X-ray photoelectron spectrometer (XPS), a Raman spectrometer, *etc.* HR-TEM images of exfoliated MoSe<sub>2</sub> nanocrystals were obtained using a JEOL JEM 2100 (200 kV) with a LaB<sub>6</sub> electron gun and a JEOL 2100 Field Emission Gun Transmission Electron Microscope. AFM images were taken using a Bruker Multimode 8. XPS measurements were carried out using a PHI Quantera

XPS. X-Ray diffraction patterns were collected using an Emperean PANalytical XRD system with reference X-ray illumination as Cu K $\alpha$  radiation at 0.154 nm. Raman measurements with an excitation laser line of 632.8 nm are performed using a LabRAM HR Raman spectrometer. Elemental analysis was performed by inductively coupled plasma-optical emission spectroscopy (ICP-OES, Perkin Elmer DV5300).

### Electrochemical characterization

The electrocatalytic activity of MoSe<sub>2</sub> nanocrystals towards the HER was evaluated using a three-electrode system using 0.5 M H<sub>2</sub>SO<sub>4</sub> aq. electrolyte bubbled with extra pure H<sub>2</sub> gas using linear sweep voltammetry. A Pt wire auxiliary electrode (BASi, MW-4130) and an Ag/AgCl reference electrode (BASi, MF-2021) preserved in 3 M aq. NaCl solution were used as counter and reference electrodes, respectively. The redox properties of the material were studied using cyclic voltammetry by applying a potential ranging from +0.2 V to -0.6 V *vs.* the Ag/AgCl reference electrode at a very slow scan rate of 2 mV s<sup>-1</sup>. All the potentials are stated after calibrating with respect to the standard reduction potential of the reversible hydrogen electrode (RHE) and further normalised in such a way that the zero current density for the Pt electrode corresponds to 0 V *vs.* the RHE. Working electrodes were fabricated in three different ways as follows.

**Drop casting.** 1 mL of as-synthesized MoSe<sub>2</sub> nanocrystals dispersed in the exfoliation mixture after centrifugation (1.60 mg mL<sup>-1</sup>) is mixed with 80  $\mu$ L of 5 wt% Nafion 117 solution (Sigma-Aldrich) and mixed thoroughly by ultra-sonication for 10 minutes. 20  $\mu$ L of this solution is drop cast onto a freshly polished gold working electrode of diameter 1.6 mm (BASi, MF-2014) and dried at room temperature, which acted as the working electrode for the dropcasting method.

**Self-assembly.** MoSe<sub>2</sub> nanocrystals were self-assembled (SA) onto a gold strip by immersing the well-cleaned Au foil in the exfoliation mixture of concentration 1.60 mg mL<sup>-1</sup> overnight after purification using a centrifugal concentrator. This was dried in a vacuum desiccator for 48 h and directly used as the working electrode for the SA method.

**Electrophoretic deposition.** Au foil to be employed as the working electrode in the direct deposition method is deployed as the cathode during the electrochemical exfoliation step. Depending on the deposition time (1–3 h) the directly deposited electrodes were named ED 1 h, ED 2 h and ED 3 h. The mass loaded for each of the electrodes was found to be 9.9  $\mu$ g cm<sup>-2</sup>, 17.9  $\mu$ g cm<sup>-2</sup>, and 23.8  $\mu$ g cm<sup>-2</sup> for ED 1 h, ED 2 h and ED 3 h, respectively. Electrophoretically deposited electrodes were directly used as working electrodes for the ED method after drying under vacuum conditions followed by washing with DI water and ethanol. ED 1 h is further washed with freshly prepared piranha solution (a mixture of H<sub>2</sub>SO<sub>4</sub> and 30% H<sub>2</sub>O<sub>2</sub> in the ratio 3 : 1) by dipping for 20, 40 and 60 s to yield electrodes named ED 1 h P1, ED 1 h P2 and ED 1 h P3 respectively. After the piranha treatment, the electrode was washed with copious amount of distilled water to completely remove the acid and oxidation products.

## Results and discussion

An electrochemical exfoliation method was employed for synthesizing MoSe<sub>2</sub> nanocrystals, starting from their bulk, by using 0.1 wt% aq. LiTFSI electrolyte under a constant applied DC potential of 5 V. During the exfoliation process, the MoSe<sub>2</sub> pellet and the FTO/gold foil were used as positive and negative electrodes, respectively. The exfoliated electrolyte solution contains a mixture of several exfoliation/oxidation/decomposition products whose composition is very complex to elucidate. However, we could see a drift of the exfoliation products towards the negative electrode as the exfoliation proceeds and a uniform coating was observed on the cathode surface. MoSe<sub>2</sub> nanocrystals dissolved in the exfoliated solution and deposited on the cathode surface are characterized by TEM and AFM analyses (Fig. 1). MoSe<sub>2</sub> nanoparticles of ~2 to 3 nm size are observed in the TEM image (Fig. 1a), which is a bit fuzzy due to the presence of the electrolyte and other anodic decomposition products. Fig. 1b reveals the hexagonal lattice of the nanoparticles present in the exfoliation mixture, and the Fast Fourier Transform (FFT) and inverse FFT (IFFT) analysis of the marked area shown in Fig. 1c and d, respectively, confirms the 2H-phase from the reflections from (110), (004), (100), (206) and (105) planes marked in Fig. 1c. Additional TEM and

HRTEM images, IFFT patterns and the energy dispersive X-ray spectrum (EDX) are shown in Fig. S2.† MoSe<sub>2</sub> nanocrystals are selectively deposited onto the counter electrode from the electrolyte solution containing exfoliated particles and decomposition products, by virtue of the applied electric field, and hence, are found to be much neater when re-dispersed in ethanol, compared to the MoSe<sub>2</sub> nanocrystals in the exfoliated solution (Fig. 1e). 90% of the particles had a very uniform diameter of ~1.8 nm (inset of Fig. 1e). Fig. 1f and g show the HRTEM and Selected Area Electron Diffraction (SAED) pattern of the highly crystalline MoSe<sub>2</sub> nanocrystals, respectively. Reflections from various planes *viz.* (207), (116), (105), and (006) are indexed in Fig. 1g. EDX spectra acquired on ED show a Mo to Se ratio of 1 : 2.3 (Fig. 1h), indicating the presence of chalcogenide terminated edges in the exfoliated nanocrystals. Further, the layer thickness of most of the exfoliated particles was found to be ≤2 nm which corresponds to three layers or less, as evident from the AFM analysis (Fig. 1i and j). MoSe<sub>2</sub> nanoparticles with a clear nanograin boundary interspersed on some highly crystalline nanosheets of 2H-MoSe<sub>2</sub> were also observed (Fig. S3†).

The powder X-ray diffraction pattern of MoSe<sub>2</sub> electro-deposited on the FTO substrate shows a (002) peak at 13.45°, close to 13.69° (ICDD reference code: 00-020-0757), indicating a slight expansion along the *c*-axis (Fig. 2a). The shift in  $2\theta$

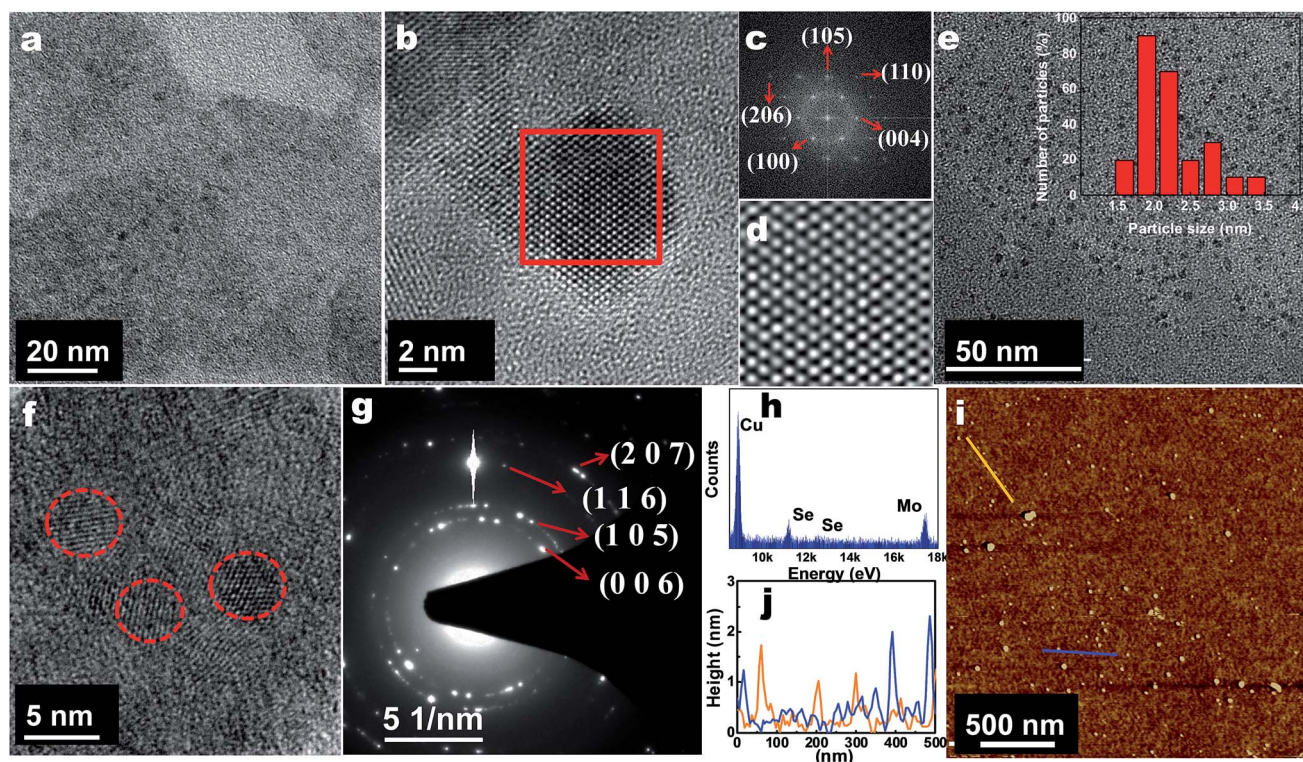


**Fig. 1** Microscopic characterization of the electrochemically exfoliated MoSe<sub>2</sub> nanocrystals. (a) TEM image of MoSe<sub>2</sub> nanocrystals as found in the exfoliation electrolyte bath. Anodic decomposition products of the electrolyte make the background fuzzy. (b) HRTEM image of a single MoSe<sub>2</sub> nanocrystal; FFT and IFFT images of the selected area in (b) are shown in (c) and (d), respectively. (e) TEM image of MoSe<sub>2</sub> nanocrystals directly deposited on the FTO substrate and re-dispersed in ethanol. The electrophoretic deposition technique purifies the nanocrystals and nearly monodisperse particle distribution around 1.8 nm is achieved as shown in the inset. (f) and (g) represent the HRTEM image and the SAED pattern, respectively, of the ED sample corresponding to the 2H phase. (h) EDX spectrum of the ED sample. (i) AFM image of the MoSe<sub>2</sub> nanocrystals. The efficiency of exfoliation into mono- to tri-layers is clearly revealed as indicated in the height profiles (j), taken along the marked lines in blue and green colours in (i).

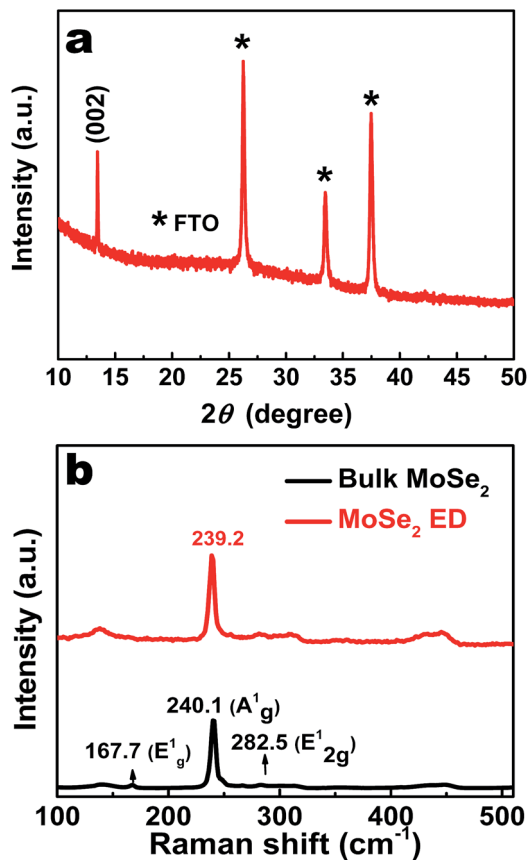


Fig. 2 Diffraction and spectroscopic characterization of exfoliated MoSe<sub>2</sub> nanocrystals. (a) Powder XRD pattern of electrodeposited MoSe<sub>2</sub> nanocrystals onto FTO after 3 h deposition time corresponds to 2H-MoSe<sub>2</sub> (ICDD Ref. code: 04-004-4471). (b) Raman spectra of bulk MoSe<sub>2</sub> and electrodeposited MoSe<sub>2</sub> nanocrystals.

corresponds to an expansion of 0.12 Å, which is very close to the expansion observed in 2H-MoSe<sub>2</sub> after Li intercalation.<sup>36</sup> The Raman spectra of bulk MoSe<sub>2</sub> and MoSe<sub>2</sub> nanocrystals electrodeposited on FTO are shown in Fig. 2b. The Raman spectrum of bulk MoSe<sub>2</sub> shows E<sub>1g</sub>, E<sub>2g</sub><sup>1</sup> modes at 167.7 and 282.5 cm<sup>-1</sup>, respectively, whereas the third in-plane vibrational mode, E<sub>2g</sub><sup>2</sup>, could not be observed with the present Raman spectrometer.<sup>37</sup> The major peak at 240.1 cm<sup>-1</sup> corresponds to out-of-plane vibrational mode, A<sub>1g</sub>. After the exfoliation, while the E<sub>1g</sub> peak disappeared (could be because the corresponding mode is forbidden in the back scattering geometry on the (0001) plane<sup>38</sup>), the A<sub>1g</sub> peak is red shifted to 239.2 cm<sup>-1</sup> for the electrochemically exfoliated MoSe<sub>2</sub> electrodeposited onto FTO. This is attributed to the softening of the vibrational mode accompanied by the reduction in layer thickness.<sup>39</sup> Apart from the Raman active vibrations from 2H-MoSe<sub>2</sub>, the electrodeposited MoSe<sub>2</sub> sample yielded Raman active vibrations corresponding to oxygen deficient molybdenum oxide (MoO<sub>3-x</sub>),<sup>40</sup> when focused on different spots (Fig. S4†). Thus the microscopic, spectroscopic and electron/X-ray diffraction analyses reveal the morphology and crystalline nature of the electrochemically exfoliated MoSe<sub>2</sub> nanocrystals and the presence of coexisting oxygen deficient Mo oxides.

The mechanism of electrochemical exfoliation is believed to be oxidative scissoring followed by large ionic incorporation.<sup>35,41</sup> Under the high applied potential of 5 V, water undergoes decomposition resulting in the formation of hydroxyl and oxygen free radicals, which act as electrochemical scissors to initiate the exfoliation process. Bonde *et al.* studied the electrochemical oxidation of MoS<sub>2</sub> resulting in the preferential edge oxidation/corrosion over the basal plane as first reported by Kautek and Gerischer in 1982.<sup>42,43</sup> In fact the edges of MoSe<sub>2</sub> do undergo an oxidative etching process resulting in oxidized Mo and Se edges similar to that of MoS<sub>2</sub>. A complete oxidation would generally result in the deactivation of electrochemical catalytic activity.<sup>42</sup> However, here, the synergistic activity of the free radical scissoring action and the bulky trifluorsulphonylimide ion (TFSI<sup>-</sup>) incorporation-induced exfoliation results in the formation of catalytically active, partially edge oxidized and core preserved MoSe<sub>2</sub> nanocrystals along with the oxidation products of Mo with +3 and +6 oxidation states.<sup>35</sup> XPS studies have been reported on the electrochemical decomposition of TFSI<sup>-</sup> anions and the major decomposition product is believed to be F<sup>-</sup> along with gaseous products like carbon dioxide.<sup>44</sup> However, such anionic species are expected to reduce the host material as widely reported for organo lithium compounds and the evolution of gaseous by-products can facilitate the exfoliation process. Hence the incorporation and decomposition of TFSI<sup>-</sup> ions can lead to a modification in the electronic structure by thinning down to mono/few layers or by varying the d electron density of Mo.

Investigation of the binding energy of the constituting elements of LiTFSI in exfoliated solution and ED will shed more light on the mechanism of exfoliation and possible incorporation of lithium into electrodeposited MoSe<sub>2</sub>. Fig. 3 represents the evolution of the binding energy of Li 1s, C 1s, N 1s and F 1s before and after electrochemical exfoliation and after electrophoretic deposition. Fig. 3a, e, and i show the evolution of the binding energy of Li 1s in LiTFSI, exfoliation solution and in the ED sample, respectively. The presence of lithium in the MoSe<sub>2</sub> samples justifies powder X-ray diffraction data, indicating slight expansion along the *c*-axis. Li 1s in pristine LiTFSI has a binding energy of 56.2 eV, which rises to 58.8 eV upon the oxidative exfoliation process. Such a high binding energy for Li 1s is very uncommon and the same component is present even in the ED sample after the cathodic deposition step. However, this could originate from the Se-containing decomposition products and it is difficult to decipher precisely, as the binding energy of Se 3d and Li 1s overlaps. Components centred around 55.2 and 51.7 eV present in Fig. 3e and i, respectively, are attributed to oxides of Li and LiF, respectively.<sup>45</sup> As the exfoliation solution is rich in fluoride ions, LiF formation is highly probable.<sup>46</sup> After the cathodic deposition, Li 1s appears at 56.1 eV indicating the presence of intercalated or deposited Li instead of oxides and fluorides in the exfoliation solution (Fig. 3i). It is interesting to note the evolution of binding energy of C 1s as shown in Fig. 3b, f and j. C 1s has a binding energy of ~293 eV in LiTFSI which undergoes decomposition resulting in the formation of hydrocarbons (284.9 and 283.8 eV) in the solution phase and part of pristine LiTFSI (292.2 eV) as shown in Fig. 3f. Interestingly,

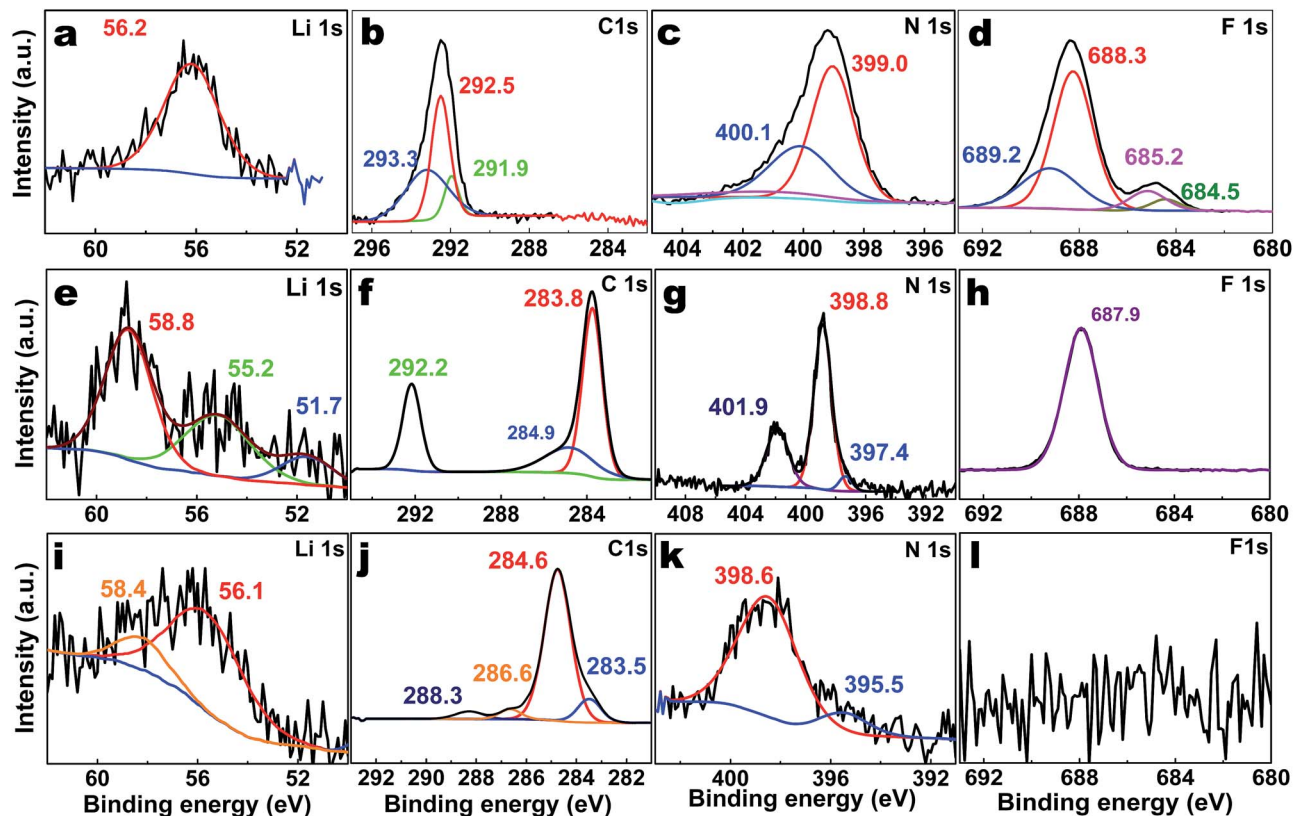


Fig. 3 XPS analysis of the constituent elements of LiTFSI upon anodic oxidation and cathodic deposition of MoSe<sub>2</sub> (onto Au). (a), (e) and (i) show the Li 1s spectra of LiTFSI, exfoliation solution and the ED sample, respectively. (b), (f) and (j) show the C 1s spectra of LiTFSI, exfoliation solution and the ED sample, respectively. (c), (g) and (k) show the N 1s spectra of LiTFSI, exfoliation solution and the ED sample, respectively and (d), (h) and (l) show the F 1s spectra of LiTFSI, exfoliation solution and the ED sample, respectively.

upon cathodic deposition, the hydrocarbons get reduced and result in the formation of olefin carbon (284.6 eV) as shown in Fig. 3j, which can facilitate the electronic communication between the active sites and the protons. Similar decomposition and reduction processes are applicable for N 1s as well (Fig. 3c, g and k). The F 1s binding energy reduces to 687.9 eV from 688.3 eV indicating the formation of fluoride ions in the electrolyte (Fig. 3d and h), which are not seen to be carried to the cathode surface during the cathodic deposition (Fig. 3l).

Understanding the chemical environment of these nanocrystals is important, especially in view of their application in electrocatalysis. XPS has been used to study their valence states and composition (Fig. 4). The XPS spectrum for the Mo 3d elemental scan for bulk MoSe<sub>2</sub> shows peaks at 228.7 and 231.9 eV, corresponding to Mo<sup>4+</sup> 3d<sub>5/2</sub> and 3d<sub>3/2</sub>, respectively, and the small peak at 230 eV is attributed to Se 3s (Fig. 4a).<sup>47</sup> Fig. 4b shows the XPS elemental scan for Se 3d in bulk MoSe<sub>2</sub>, in which peaks at 54.4 and 55.2 eV are attributed to Se 3d<sub>5/2</sub> and 3d<sub>3/2</sub>, respectively. Fig. 4c and d represent the Mo 3d and Se 3d elemental scans, respectively, for the ED samples. Peaks centred around 228.9 and 231.8 eV correspond to Mo<sup>4+</sup> 3d<sub>5/2</sub> and 3d<sub>3/2</sub>, respectively. The observed significant broadening of Mo 3d spectra along with a slight shift in the binding energy might be caused by the traces of the 1T phase.<sup>48</sup> The major components of the Mo 3d spectra of ED show only a small difference in the

binding energy (+0.1 eV for 3d<sub>5/2</sub> and 3d<sub>3/2</sub>, respectively) compared to bulk MoSe<sub>2</sub> spectra, and prove that the oxidation state of Mo has not changed though it is vulnerable to oxidation

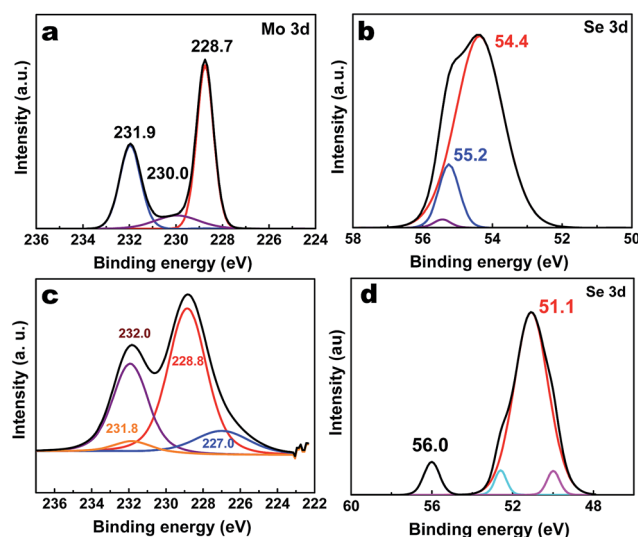


Fig. 4 XPS spectra; (a) & (c) represent the XPS elemental scans for Mo 3d of bulk and ED MoSe<sub>2</sub> samples, respectively, and (b) and (d) correspond to XPS elemental scans for Se 3d of bulk and ED MoSe<sub>2</sub> samples, respectively.

under the applied positive potential. Furthermore, lithiation has not resulted in huge phase transformation to the metallic 1T phase as well, as evident from the low intensity of the respective Mo 3d doublet observed at the lower binding energy. This reluctance for the complete phase transformation accompanied by lithiation could be due to the presence of coexisting oxygen deficient molybdenum oxides ( $\text{MoO}_{3-x}$ ).<sup>25</sup> XPS evidence, wherein broadening extending beyond 232.0 eV corresponding to higher oxidation states of Mo (Fig. 4c), and the observed Raman data (Fig. S4†) very well corroborate this possibility.<sup>24,40</sup> Such partial oxidation can potentially improve the electronic conductivity of TMDs.<sup>24,49</sup> Finally, Fig. 4d shows the Se 3d of ED  $\text{MoSe}_2$ . There is huge lowering in the binding energy of Se 3d electrons to 51.1 eV and this could be attributed to the formation of terminal  $\text{Se}_2^{2-}$  and  $\text{Se}^{2-}$  upon cathodic deposition, similar to the reports on the lowering of binding energy of S 2p orbitals in  $\text{MoS}_2$ .<sup>50,51</sup> Such uncompensated chalcogenide edges are reported to show improved electrocatalytic activity.<sup>50</sup> The small component at 56.0 eV is attributed to the presence of traces of lithium.

The physico-chemical characterization of the electrochemically exfoliated and electrodeposited  $\text{MoSe}_2$  nanocrystals reveals that they possess several structural and chemical features essential for an ideal electrocatalyst for the HER *viz.*, a high edge to basal plane ratio, electrochemically active  $\text{Se}^{2-}/\text{Se}_2^{2-}$  terminals and lithiation induced catalytically active defect sites, all in one. To check the electrochemical performance of the synthesized  $\text{MoSe}_2$  nanocrystals, we fabricated the working electrodes in three different ways. First, the exfoliated electrolyte solution is dried in a rotavapor and the residual powder is dropcast on a gold working electrode and cyclic voltammograms (CV) were recorded starting with a cathodic potential sweep from 0.2 to  $-0.8$  V *vs.* the Ag/AgCl (Fig. S5a†) in sodium phosphate buffer solution (pH = 7) at a scan rate of  $100 \text{ mV s}^{-1}$ . The first cycle of CV showed a sharp reduction peak at 0.39 V and a weak peak at 0.33 V and poor hydrogen evolution was observed upon further scanning towards higher negative potentials. Upon continuing the CV scans, the hydrogen evolution was found to further diminish drastically and a new broad reduction peak centred around 0.62 V started to appear. The major reduction peak could be corresponding to the reduction of oxidized Mo at the basal plane, and the two minor reduction peaks could be due to the reduction of oxidized Mo situated at the edges and  $\text{Mo}^{6+/3+}$  species coming from the dissolved oxides of Mo during the electrochemical exfoliation process.<sup>42</sup> Hence, the electrode prepared through dropcasting of the exfoliated solution does not offer promising electrocatalytic performance, majorly due to the presence of oxide contaminants. However, when the electrocatalytic activity is tested in  $0.5 \text{ M H}_2\text{SO}_4$ , this electrode showed an onset potential (arbitrarily fixed as the potential corresponding to a current density of  $1 \text{ mA cm}^{-2}$ ) of 404.1 mV *vs.* the RHE with a Tafel slope of  $42.5 \text{ mV dec}^{-1}$  (Fig. S5c and d†). With a low Tafel slope, this material exhibits good potential to be an excellent electrocatalyst for the HER.

The electrocatalytic activity of transition metal dichalcogenides (TMDs) is best demonstrated on gold substrates.<sup>51-54</sup> Nanoparticles and nanoparticles interspersed on nanosheets of

TMDs adhered to Au have been reported to show impressive electrocatalytic activity. Hence, we prepared  $\text{MoSe}_2$  nanocrystals self-assembled on gold foil (SA) by incubating overnight. Surprisingly, the electrochemical performance of the SA electrode was found to be dramatically improved compared to that of the electrode fabricated through drop casting. SA shows an onset potential of 104.5 mV *vs.* the RHE with an overpotential of 153.1 mV *vs.* the RHE at a current density of  $10 \text{ mA cm}^{-2}$  (Fig. 5a). Earlier, the enhanced electrocatalytic activity of  $\text{MoS}_2$  nanocrystals self-assembled on gold was attributed to the electrocatalytically active sulphur rich composition of the loaded catalyst.<sup>51</sup> However, as far as  $\text{MoSe}_2$  is concerned, both Mo and Se edges are equally active towards the electrocatalysis; hence self-assembly might not be the best possible option for the electrode fabrication.<sup>31</sup> Electrophoretic deposition of exfoliated  $\text{MoSe}_2$  nanocrystals directly onto the gold surface for 3 h gives detectable amounts of deposition unlike self-assembly driven electrode fabrication. The CV obtained for the electrochemically deposited sample (Fig. S5b†) shows no sign of oxidation products of  $\text{MoSe}_2$  deposited onto the cathode surface. Apart from the absence of a reduction peak during the cathodic sweep, the cathodic current remained the same until the 30th cycle. Thus, the CV results confirm that the electrophoretic deposition step results in the deposition of pure  $\text{MoSe}_2$  nanocrystals as already indicated by the TEM analysis. However, the electrocatalytic activity of the as-prepared ED exhibits an onset potential of 358.1 mV *vs.* the RHE and a Tafel slope of  $94.0 \text{ mV dec}^{-1}$ , much inferior to that of the self-assembly driven electrode (SA). This could have been stemmed from the thick deposition of the active material or co-deposition of unwanted electrolyte decomposition products. To address this, the thickness of the coating was optimized by varying the deposition time *viz.* 3 h, 2 h and 1 h to yield electrodes namely ED 3 h, ED 2 h and ED 1 h, respectively. AFM images and the depth correlation on the entire scanned area show that the thickness of deposition varies from  $\sim 11 \mu\text{m}$  to  $\sim 350 \text{ nm}$  as the deposition time varied from 3 h to 1 h (Fig. S6†). This reduction in the thickness is well reflected in the electrochemical performance as shown in the ESI, Fig. S7.† Optimization of the thickness brought in dramatic improvement in electrocatalytic activity; the onset potential and Tafel slope were found to be 161.5 *vs.* the RHE and  $74 \text{ mV dec}^{-1}$ , respectively, for the pristine ED 1 h sample. Even when the thickness was reduced to 750 nm for the ED 2 h sample, the mechanism of hydrogen evolution is believed to be the same as that of ED 1 h as evident from the observed similar Tafel slope ( $73 \text{ mV dec}^{-1}$ ). A further improvement is anticipated by the removal of impeding electrolyte decomposition products on the surface of the electrode. This is achieved by washing the ED 1 h sample by dipping in freshly prepared piranha solution for 20 s and washing with copious amount of distilled water to get ED 1 h P1. This cleaning procedure is continued until 40 and 60 s to get electrodes ED 1 h P2 and ED 1 h P3, respectively. XPS analysis was carried out on the piranha-treated samples and the elemental composition showing the progressive removal of organic decomposition products is tabulated in the ESI, Table S1.† However, the percentage composition of Li on the electrode was found to

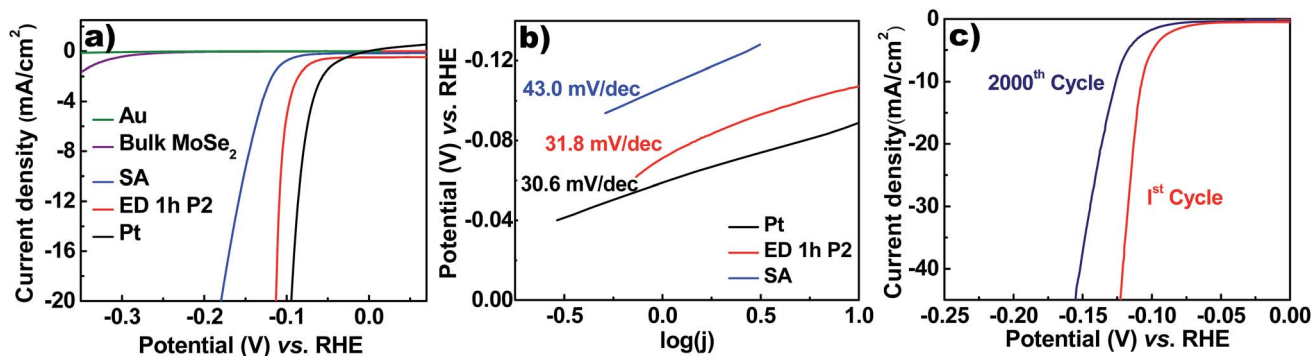


Fig. 5 Electrochemical characterization of the electrochemically exfoliated MoSe<sub>2</sub> nanocrystals. (a) Polarization curves obtained for exfoliated MoSe<sub>2</sub>-modified Au electrodes by direct electrophoretic deposition (ED 1 h P2), self-assembly (SA) and bulk MoSe<sub>2</sub> at a scan rate of 2 mV s<sup>-1</sup> in 0.5 M aq. H<sub>2</sub>SO<sub>4</sub> electrolyte. Polarization curves for the Au substrate and Pt are shown for comparison. (b) Tafel slopes obtained for the best performing electrodes. (c) Polarization curve obtained for ED 1 h P2 after 2000 potential sweeps is compared with the first cycle to show the stability of catalytic activity.

increase with each wash. This lithium could be either intercalated or interstitially substituted and cannot be coming from LiF, the inorganic electrolyte decomposition product, as it has not been carried during the cathodic deposition. With each piranha wash, carbon and nitrogen based decomposition products are leached off and the lithium content remains the same and eventually ends up in an enhanced percentage composition of lithium. This lithium composition seems to have a critical role in significant enhancement of the electrocatalytic activity, as evident from the onset potential and the Tafel plot (Fig. S8†). ED 1 h showed an onset potential of 161.5 mV vs. the RHE which was lowered to 94.5 mV vs. the RHE after the first piranha wash for the sample named ED 1 h P1. A corresponding decrease in the Tafel slope and increase in the exchange current density were also observed, from 74 mV dec<sup>-1</sup> and  $1.1 \times 10^{-3}$  mA cm<sup>-2</sup> to 55.5 mV dec<sup>-1</sup> and  $2.1 \times 10^{-2}$  mA cm<sup>-2</sup>, respectively. The best electrochemical catalytic activity was shown by ED 1 h P2. This electrode exhibited a low onset potential of 70.9 mV vs. the RHE with an overpotential of 107.2 mV vs. the RHE (at  $j = 10$  mA cm<sup>-2</sup>) (Fig. 5a), an ultra-low Tafel slope of 31.8 mV dec<sup>-1</sup> (Fig. 5b) and an excellent exchange current density of  $2.0 \times 10^{-2}$  mA cm<sup>-2</sup>, making it an exceptionally good electrocatalyst for the HER (Table 1), one among the best reported electrocatalysts (Table 2). A polarization curve

has also been obtained in terms of the gravimetric current density (Fig. S9†). The electrocatalyst shows good cycling stability, wherein the activity has not been much compromised after 2000 cycles of CV scans (Fig. 5c). Thus MoSe<sub>2</sub> nanocrystals with a high catalytically active edge to inert basal plane ratio, co-existing MoO<sub>3-x</sub> and resultant enhanced conductivity, lithiation-induced active sites and electrochemically active uncompensated selenide edges synergistically act resulting in the exceptional electrocatalytic activity. The possibility of any Pt contamination of the electrocatalyst contributing to the electrochemical activity has been ruled out by ICP-OES estimation of metal ions (Table S2†).

Although co-deposition of Li ions and MoSe<sub>2</sub> nanocrystals onto conducting substrates results in the formation of lithiated MoSe<sub>2</sub> nanocrystals with the emergence of new active sites, they do not transform from 2H to 1T/1T' phase. The stability of the lithiated phase is another debatable scenario here. The stability could originate from the formation of an SEI like the passivation layer on the surface of the electrocatalyst. An alternate possibility is about the Li<sup>+</sup> substitution of Mo<sup>6+</sup> in the co-existing MoO<sub>3-x</sub> phase interstitially. This can create anion vacancies and the trapped free electrons in such anion vacancies can impart metallic conductivity to the material resulting in the enormous enhancement in the electrocatalytic activity.<sup>49</sup> In

Table 1 Comparison of the electrocatalytic activity towards the HER for various electrodes fabricated using electrochemically exfoliated MoSe<sub>2</sub> nanocrystals

Material	Onset potential (mV vs. the RHE) at 1 mA cm <sup>-2</sup>	$\eta$ (mV vs. the RHE) at 10 mA cm <sup>-2</sup>	Tafel slope (mV dec <sup>-1</sup> )	Exchange current density (mA cm <sup>-2</sup> )
Dropcast	404.1	—	42.5	$2.0 \times 10^{-9}$
SA	104.5	151.3	43.0	$2.4 \times 10^{-3}$
ED 3 h	358.1	463.1	103.7	$1.9 \times 10^{-4}$
ED 2 h	231.4	318.0	73.0	$7.7 \times 10^{-4}$
ED 1 h	161.5	250.8	74.0	$1.1 \times 10^{-3}$
ED 1 h P1	94.5	163.4	55.5	$2.1 \times 10^{-2}$
ED 1 h P2	70.9	107.2	31.8	$2.0 \times 10^{-2}$
ED 1 h P3	132.0	219.4	70.3	$1.5 \times 10^{-2}$

Table 2 Comparison of the electrocatalytic activity of exfoliated MoSe<sub>2</sub> nanocrystals towards the HER with the best electrocatalysts reported

Catalyst	Synthesis method	Electrolyte	Onset potential (mV vs. the RHE)	$\eta$ (mV vs. the RHE) at 10 mA cm <sup>-2</sup>	Tafel slope (mV dec <sup>-1</sup> )
MoS <sub>2</sub> <sup>6</sup>	CVD	0.5 M H <sub>2</sub> SO <sub>4</sub>	150	187	43
MoSe <sub>2</sub> <sup>7</sup>	CVD	0.5 M H <sub>2</sub> SO <sub>4</sub>	110	250	59.8
MoS <sub>2</sub> /CoSe <sub>2</sub> <sup>8</sup>	Solvo-thermal	0.5 M H <sub>2</sub> SO <sub>4</sub>	11	68	36
N <sub>2</sub> H <sub>4</sub> treated MoO <sub>x</sub> /MoS <sub>2</sub> nanowires <sup>9</sup>	CVD	0.5 M H <sub>2</sub> SO <sub>4</sub>	100	—	50
Cu-Ti <sup>10</sup>	Arc melting	0.1 M KOH	70 to 115	—	110
S-Doped MoSe <sub>2</sub> <sup>11</sup>	Reflux method	0.5 M H <sub>2</sub> SO <sub>4</sub>	90	~100	60
Strained & S vacant MoS <sub>2</sub> <sup>12</sup>	CVD	0.5 M H <sub>2</sub> SO <sub>4</sub>	—	170	60
MoSe <sub>2</sub> /graphene <sup>13</sup>	CVD	0.5 M H <sub>2</sub> SO <sub>4</sub>	50	159	61
CoPS <sup>14</sup>	Thermal evaporation/ hydrothermal	0.5 M H <sub>2</sub> SO <sub>4</sub>	—	61	48
CNT@MoSe <sub>2</sub> <sup>15</sup>	Solvo-thermal	0.5 M H <sub>2</sub> SO <sub>4</sub>	70	178	58
MoSe <sub>2</sub> nanocrystals (present work)	Electrochemical	0.5 M H <sub>2</sub> SO <sub>4</sub>	70.9	107.2	31.8

order to confirm the critical role of *in situ* lithiation in enhancing the electrochemical activity of the ED sample, MoSe<sub>2</sub> nanocrystals are electrochemically exfoliated and deposited using a BMImCl-based aq. electrolyte instead of LiTFSI under similar conditions to those for ED 1 h and characterized thoroughly to verify the size and the phase. These nanocrystals were found to have a slightly higher particle size distribution around 3.2 nm (Fig. S10†). This increase in the particle size is in accordance with our previous report on the electrochemical tunable synthesis of MoS<sub>2</sub> nanocrystals using the same electrolytes.<sup>35</sup> Lattice expansion observed in electrophoretic deposited MoSe<sub>2</sub> samples was not observed in MoSe<sub>2</sub> nanocrystals synthesised using an aq. BMImCl-based electrolyte as evident from the (002) reflection at 13.65° (Fig. S11†) much closer to the reported values (ICDD reference code: 00-020-0757). Furthermore, the Raman spectrum shows that the sample is in the semi-conducting 2H phase (Fig. S12†). The electrocatalytic activity of these MoSe<sub>2</sub> nanocrystals is studied (Fig. S13†) under similar conditions previously discussed. MoSe<sub>2</sub> nanocrystals synthesised using BMImCl show an overpotential of 148.2 mV vs. the RHE, which is nearly 50 mV higher than that of the ED 1 h P2 electrode. The Tafel slope was found to be 46.6 mV dec<sup>-1</sup>, much higher than that of the ED 1 h P2 electrode.

## Conclusions

To summarize, monodisperse single/few-layered MoSe<sub>2</sub> nanocrystals are directly deposited onto gold foil through a facile electrochemical exfoliation process. Upon oxidative etching treatment using piranha solution, the electrode exhibited exceptionally high HER activity with a very low Tafel slope of 31.8 mV dec<sup>-1</sup>, making it one among the best electrocatalysts reported so far. The enhanced electrocatalytic activity is attributed to the synergistic advantages of the electrodeposited sample resulting from various factors such as the new active sites emerging by virtue of a high edge to basal plane ratio, electrochemically active uncompensated chalcogenide edges, electrochemical lithiation induced new active sites and enhanced electronic conductivity due to the co-existing MoO<sub>3-x</sub>, all acting in one step. Such a one-step process can be

extended to other TMD family members that could result in interesting physico-chemical properties for useful applications in energy conversion and sensors.

## Acknowledgements

D. D. acknowledges the support from the Council of Scientific & Industrial Research (CSIR), Government of India, for the fellowship. A. A. acknowledges the Department of Science and Technology (DST), Government of India, for the INSPIRE Scholarship. This work was supported by the Indian Institute of Science Education & Research Thiruvananthapuram, through a startup grant to M. M. S. The authors thank N. Ravishankar for the HRTEM analysis. Abhishek K. Singh, T. N. Narayanan, Deya Das and Vineesh Thazhevedu are greatly acknowledged for fruitful discussions.

## Notes and references

- P. C. K. Vesborg, B. Seger and I. Chorkendorff, *J. Phys. Chem. Lett.*, 2015, **6**, 951.
- A. B. Laursen, S. Kegnaes, S. Dahl and I. Chorkendorff, *Energy Environ. Sci.*, 2012, **5**, 5577.
- B. E. Conway and B. V. Tilak, *Electrochim. Acta*, 2002, **47**, 3571.
- E. J. Popczun, C. G. Read, C. W. Roske, N. S. Lewis and R. E. Schaak, *Angew. Chem., Int. Ed.*, 2014, **53**, 5427.
- M. Caban-Acevedo, M. L. Stone, J. R. Schmidt, J. G. Thomas, Q. Ding, H.-C. Chang, M.-L. Tsai, J.-H. He and S. Jin, *Nat. Mater.*, 2015, **14**, 1245.
- W. Liu, E. Hu, H. Jiang, Y. Xiang, Z. Weng, M. Li, Q. Fan, X. Yu, E. I. Altman and H. Wang, *Nat. Commun.*, 2016, **7**, 10771.
- Q. Lu, G. S. Hutchings, W. Yu, Y. Zhou, R. V. Forest, R. Tao, J. Rosen, B. T. Yonemoto, Z. Cao, H. Zheng, J. Q. Xiao, F. Jiao and J. G. Chen, *Nat. Commun.*, 2015, **6**, 6567.
- J. R. McKone, B. F. Sadler, C. A. Werlang, N. S. Lewis and H. B. Gray, *ACS Catal.*, 2013, **3**, 166.
- D. Mukherjee, P. M. Austeria and S. Sampath, *ACS Energy Lett.*, 2016, **1**, 367.

- 10 B. Hinnemann, P. G. Moses, J. Bonde, K. P. Jørgensen, J. H. Nielsen, S. Horch, I. Chorkendorff and J. K. Nørskov, *J. Am. Chem. Soc.*, 2005, **127**, 5308.
- 11 J. D. Benck, T. R. Hellstern, J. Kibsgaard, P. Chakthranont and T. F. Jaramillo, *ACS Catal.*, 2014, **4**, 3957.
- 12 S. Mao, Z. Wen, S. Ci, X. Guo, K. Ostrikov and J. Chen, *Small*, 2015, **11**, 414.
- 13 D. Kong, H. Wang, J. J. Cha, M. Pasta, K. J. Koski, J. Yao and Y. Cui, *Nano Lett.*, 2013, **13**, 1341.
- 14 H. Wang, Z. Lu, S. Xu, D. Kong, J. J. Cha, G. Zheng, P.-C. Hsu, K. Yan, D. Bradshaw, F. B. Prinz and Y. Cui, *Proc. Natl. Acad. Sci. U. S. A.*, 2013, **110**, 19701.
- 15 J. Kibsgaard, Z. Chen, B. N. Reinecke and T. F. Jaramillo, *Nat. Mater.*, 2012, **11**, 963.
- 16 Q. Ji, Y. Zhang, J. Shi, J. Sun, Y. Zhang and Z. Liu, *Adv. Mater.*, 2016, **28**, 6207.
- 17 H. Vrubel, D. Merki and X. Hu, *Energy Environ. Sci.*, 2012, **5**, 6136.
- 18 G. Ye, Y. Gong, J. Lin, B. Li, Y. He, S. T. Pantelides, W. Zhou, R. Vajtai and P. M. Ajayan, *Nano Lett.*, 2016, **16**, 1097.
- 19 J. Xie, H. Zhang, S. Li, R. Wang, X. Sun, M. Zhou, J. Zhou, X. W. Lou and Y. Xie, *Adv. Mater.*, 2013, **25**, 5807.
- 20 X. Ge, L. Chen, L. Zhang, Y. Wen, A. Hirata and M. Chen, *Adv. Mater.*, 2014, **26**, 3100.
- 21 C. Xu, S. Peng, C. Tan, H. Ang, H. Tan, H. Zhang and Q. Yan, *J. Mater. Chem. A*, 2014, **2**, 5597.
- 22 K. Xu, F. Wang, Z. Wang, X. Zhan, Q. Wang, Z. Cheng, M. Safdar and J. He, *ACS Nano*, 2014, **8**, 8468.
- 23 J. Deng, H. Li, J. Xiao, Y. Tu, D. Deng, H. Yang, H. Tian, J. Li, P. Ren and X. Bao, *Energy Environ. Sci.*, 2015, **8**, 1594.
- 24 Z. Chen, D. Cummins, B. N. Reinecke, E. Clark, M. K. Sunkara and T. F. Jaramillo, *Nano Lett.*, 2011, **11**, 4168.
- 25 D. R. Cummins, U. Martinez, R. Koppera, D. Voiry, A. Martinez-Garcia, J. Jasinski, D. Kelly, M. Chhowalla, A. D. Mohite, M. K. Sunkara and G. Gupta, *J. Phys. Chem. C*, 2015, **119**, 22908.
- 26 D. R. Cummins, U. Martinez, A. Sherehiy, R. Koppera, A. Martinez-Garcia, R. K. Schulze, J. Jasinski, J. Zhang, R. K. Gupta, J. Lou, M. Chhowalla, G. Sumanasekera, A. D. Mohite, M. K. Sunkara and G. Gupta, *Nat. Commun.*, 2016, **7**, 11857.
- 27 Z. Liu, N. Li, H. Zhao and Y. Du, *J. Mater. Chem. A*, 2015, **3**, 19706.
- 28 Y. Li, H. Wang, L. Xie, Y. Liang, G. Hong and H. Dai, *J. Am. Chem. Soc.*, 2011, **133**, 7296.
- 29 J. Duan, S. Chen, B. A. Chambers, G. G. Andersson and S. Z. Qiao, *Adv. Mater.*, 2015, **27**, 4234.
- 30 S. S. Chou, N. Sai, P. Lu, E. N. Coker, S. Liu, K. Artyushkova, T. S. Luk, B. Kaehr and C. J. Brinker, *Nat. Commun.*, 2015, **6**, 8311.
- 31 C. Tsai, K. Chan, F. Abild-Pedersen and J. K. Nørskov, *Phys. Chem. Chem. Phys.*, 2014, **16**, 13156.
- 32 M. A. Lukowski, A. S. Daniel, C. R. English, F. Meng, A. Forticaux, R. J. Hamers and S. Jin, *Energy Environ. Sci.*, 2014, **7**, 2608.
- 33 U. Gupta, B. S. Naidu, U. Maitra, A. Singh, S. N. Shirodkar, U. V. Waghmare and C. N. R. Rao, *APL Mater.*, 2014, **2**, 092802.
- 34 D. Damien, B. Babu, T. N. Narayanan, A. L. Reddy, P. M. Ajayan and M. M. Shaijumon, *Graphene*, 2013, **1**, 37.
- 35 D. Gopalakrishnan, D. Damien, B. Li, H. Gullappalli, V. K. Pillai, P. M. Ajayan and M. M. Shaijumon, *Chem. Commun.*, 2015, **51**, 6293.
- 36 J. Zheng, H. Zhang, S. Dong, Y. Liu, C. Tai Nai, H. Suk Shin, H. Young Jeong, B. Liu and K. Ping Loh, *Nat. Commun.*, 2014, **5**, 2295.
- 37 H. Terrones, E. D. Corro, S. Feng, J. M. Poumirol, D. Rhodes, D. Smirnov, N. R. Pradhan, Z. Lin, M. A. T. Nguyen, A. L. Elías, T. E. Mallouk, L. Balicas, M. A. Pimenta and M. Terrones, *Sci. Rep.*, 2014, **4**, 4215.
- 38 G. L. Frey, R. Tenne, M. J. Matthews, M. S. Dresselhaus and G. Dresselhaus, *Phys. Rev. B: Condens. Matter Mater. Phys.*, 1999, **60**, 2883.
- 39 S. Tongay, J. Zhou, C. Ataca, K. Lo, T. S. Matthews, J. Li, J. C. Grossman and J. Wu, *Nano Lett.*, 2012, **12**, 5576.
- 40 M. A. Camacho-López, L. Escobar-Alarcón, M. Picquart, R. Arroyo, G. Córdoba and E. Haro-Poniatowski, *Opt. Mater.*, 2011, **33**, 480.
- 41 J. Lu, J.-x. Yang, J. Wang, A. Lim, S. Wang and K. P. Loh, *ACS Nano*, 2009, **3**, 2367.
- 42 J. Bonde, P. G. Moses, T. F. Jaramillo, J. K. Nørskov and I. Chorkendorff, *Faraday Discuss.*, 2009, **140**, 219.
- 43 W. Kautek and H. Gerischer, *Surf. Sci.*, 1982, **119**, 46.
- 44 E. Krämer, T. Schedlbauer, B. Hoffmann, L. Terborg, S. Nowak, H. J. Gores, S. Passerini and M. Winter, *J. Electrochem. Soc.*, 2013, **160**, A356.
- 45 R. Dedryvère, S. Leroy, H. Martinez, F. Blanchard, D. Lemordant and D. Gonbeau, *J. Phys. Chem. B*, 2006, **110**, 12986.
- 46 J.-N. Chen and J. W. Rabalais, *Surf. Sci.*, 1986, **176**, L879.
- 47 X. Wang, Y. Gong, G. Shi, W. L. Chow, K. Keyshar, G. Ye, R. Vajtai, J. Lou, Z. Liu, E. Ringe, B. K. Tay and P. M. Ajayan, *ACS Nano*, 2014, **8**, 5125.
- 48 A. Ambrosi, Z. Sofer and M. Pumera, *Chem. Commun.*, 2015, **51**, 8450.
- 49 S. K. Deb and J. A. Chopoorian, *J. Appl. Phys.*, 1966, **37**, 4818.
- 50 M.-R. Gao, J.-X. Liang, Y.-R. Zheng, Y.-F. Xu, J. Jiang, Q. Gao, J. Li and S.-H. Yu, *Nat. Commun.*, 2015, **6**, 5982.
- 51 T. Wang, L. Liu, Z. Zhu, P. Papakonstantinou, J. Hu, H. Liu and M. Li, *Energy Environ. Sci.*, 2013, **6**, 625.
- 52 T. F. Jaramillo, K. P. Jørgensen, J. Bonde, J. H. Nielsen, S. Horch and I. Chorkendorff, *Science*, 2007, **317**, 100.
- 53 D. Gopalakrishnan, D. Damien and M. M. Shaijumon, *ACS Nano*, 2014, **8**, 5297.
- 54 J. Shi, D. Ma, G.-F. Han, Y. Zhang, Q. Ji, T. Gao, J. Sun, X. Song, C. Li, Y. Zhang, X.-Y. Lang, Y. Zhang and Z. Liu, *ACS Nano*, 2014, **8**, 10196.